TRANSPARENT PROCESS

OPEN ACCESS

Phase separation of 53BP1 determines liquid-like behavior of DNA repair compartments

Sinan Kilic[1] (iD), Aleksandra Lezaja[1,2], Marco Gatti[1], Eliana Bianco[1,2,†], Jone Michelena[1], Ralph Imhof[1] & Matthias Altmeyer[1,*] (iD)

Abstract

The DNA damage response (DDR) generates transient repair compartments to concentrate repair proteins and activate signaling factors. The physicochemical properties of these spatially confined compartments and their function remain poorly understood. Here, we establish, based on live cell microscopy and CRISPR/Cas9-mediated endogenous protein tagging, that 53BP1-marked repair compartments are dynamic, show droplet-like behavior, and undergo frequent fusion and fission events. 53BP1 assembly, but not the upstream accumulation of γH2AX and MDC1, is highly sensitive to changes in osmotic pressure, temperature, salt concentration and to disruption of hydrophobic interactions. Phase separation of 53BP1 is substantiated by optoDroplet experiments, which further allowed dissection of the 53BP1 sequence elements that cooperate for light-induced clustering. Moreover, we found the tumor suppressor protein p53 to be enriched within 53BP1 optoDroplets, and conditions that disrupt 53BP1 phase separation impair 53BP1-dependent induction of p53 and diminish p53 target gene expression. We thus suggest that 53BP1 phase separation integrates localized DNA damage recognition and repair factor assembly with global p53-dependent gene activation and cell fate decisions.

See also: **R Piccinno et al** (August 2019)

Introduction

Detection of DNA double-strand breaks (DSBs) and their faithful repair is crucial to avoid loss of genetic information and counter chromosome translocations and genomic instability. Consequently, defects in the DNA damage response (DDR) are associated with neurodegeneration, cancer, and aging, and genomic instability is a hallmark of most tumors (Jackson & Bartek, 2009). The DDR is initiated at DNA break sites by the ATM kinase, which phosphorylates histone variant H2AX to generate γH2AX (Shiloh & Ziv, 2013; Blackford & Jackson, 2017). The adaptor protein MDC1 binds γH2AX to assemble the ubiquitin E3 ligases RNF8 and RNF168 and recruit 53BP1 (Jungmichel & Stucki, 2010; Lukas et al, 2011b; Polo & Jackson, 2011; Panier & Boulton, 2014; Pellegrino & Altmeyer, 2016; Schwertman et al, 2016; Wilson & Durocher, 2017). 53BP1 generates sizeable chromatin domains, which scaffold the assembly of downstream effectors and shield DNA lesions against excessive nucleolytic digestion. Restrained resection is achieved by 53BP1-dependent recruitment of RIF1, REV7, and the Shieldin complex (Dev et al, 2018; Findlay et al, 2018; Ghezraoui et al, 2018; Gupta et al, 2018; Mirman et al, 2018; Noordermeer et al, 2018; Setiaputra & Durocher, 2019). Additionally, 53BP1 promotes cell cycle checkpoint signaling in response to DNA damage (DiTullio et al, 2002; Fernandez-Capetillo et al, 2002; Wang et al, 2002; Brummelkamp et al, 2006; Cuella-Martin et al, 2016). How 53BP1 integrates local DNA damage recognition with global checkpoint responses and why such a multilayered multi-protein assembly at DNA break sites is required to safeguard genome stability is not well understood.

Liquid–liquid phase separation has recently emerged as mechanism to dynamically sub-divide the intracellular space (Hyman et al, 2014; Alberti, 2017; Banani et al, 2017; Shin & Brangwynne, 2017). Phase separation relies on multivalent weak interactions, often through intrinsically disordered protein sequences. Such interactions retain a larger conformational flexibility compared to interactions through complementary protein domain surfaces and induced fit (Aguzzi & Altmeyer, 2016; Boeynaems et al, 2018). Besides the nucleolus, nuclear speckles, and RNA granules, also silent heterochromatin domains were recently shown to phase separate within the nucleus (Larson et al, 2017; Strom et al, 2017). Moreover, phase separation occurs at gene promoters and super-enhancers (Boehning et al, 2018; Boija et al, 2018; Lu et al, 2018; Sabari et al, 2018). To which extent other chromatin domains rely on phase separation for

1   Department of Molecular Mechanisms of Disease, University of Zurich, Zurich, Switzerland
2   Cancer Biology PhD Program, Life Science Zurich Graduate School, Zurich, Switzerland
    *Corresponding author. Tel: + 41 44 63 55 491; E-mail: matthias.altmeyer@uzh.ch
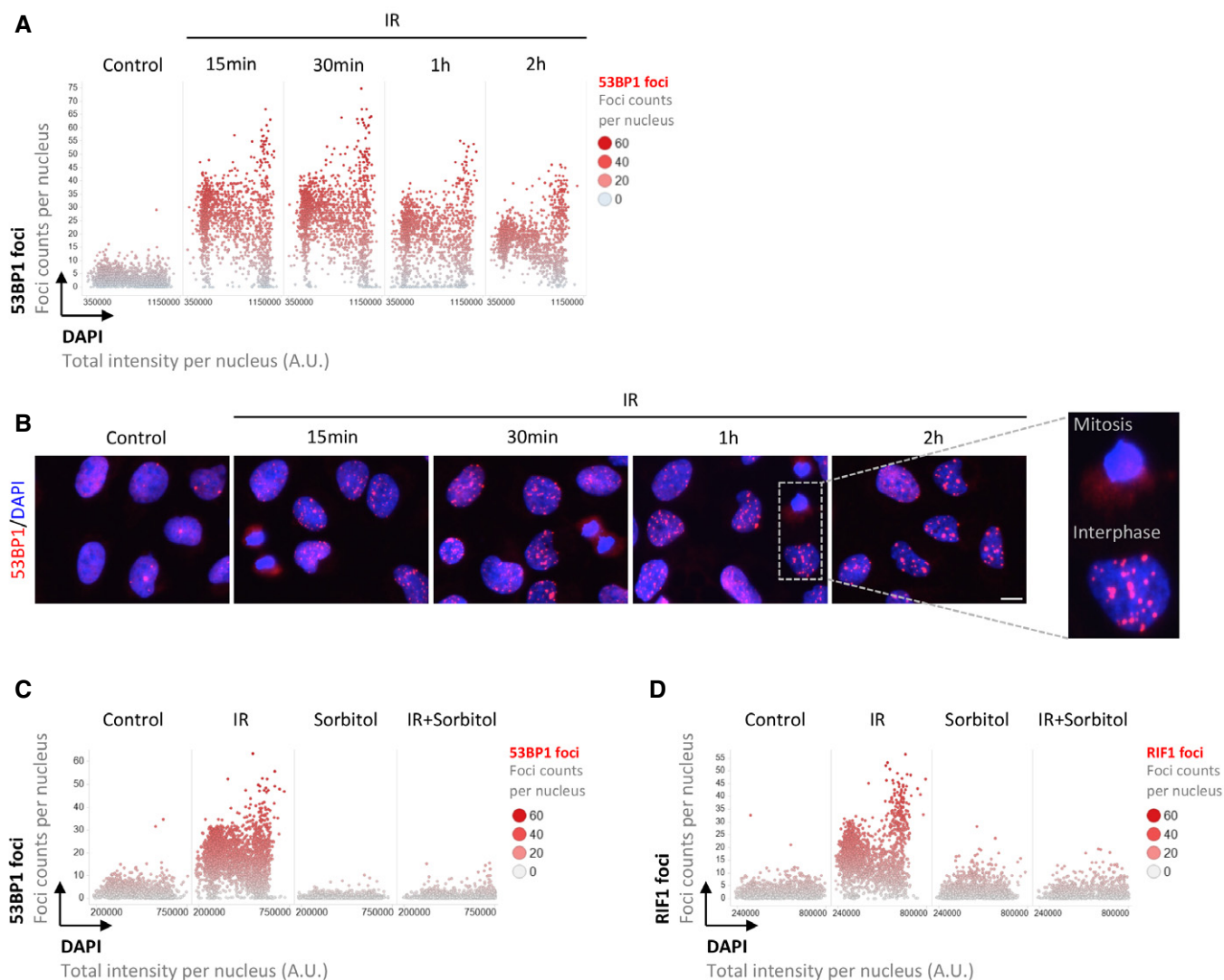   †Present address: Institute of Biochemistry, ETH Zurich, Zurich, Switzerland

Figure 1. The 53BP1 repair compartment is sensitive to hyperosmotic stress.

A   Asynchronously growing human U-2 OS cells were treated with 0.5 Gy of IR, allowed to recover for the indicated time periods, and stained for 53BP1 and DNA content for cell cycle resolved quantification of 53BP1 foci in individual cells by QIBC.

B   Representative images from the QIBC analysis in (A). Scale bars, 10 μm.

C   Cells were treated with 0.5 Gy of IR in absence or presence of 0.4 M sorbitol, fixed 1 h later, and 53BP1 assembly at DSBs was analyzed by QIBC.

D   Treatments as in (C); RIF1 accumulation at DSBs was analyzed by QIBC.

their spatio-temporal confinement and for their biological functions is a matter of intense investigation.

Although the key upstream signals for 53BP1 recruitment to sites of DNA damage are well defined, 53BP1 assembly can also be uncoupled from upstream events indicating that the hierarchical cascade of the DDR allows regulation at intermediate levels. For instance, 53BP1 assembly is precluded during mitosis, when CDK activity is high and chromosomes are heavily condensed, even though the upstream signaling and the recruitment of MDC1 are unaffected (Giunta *et al*, 2010; Orthwein *et al*, 2014). Conversely, 53BP1 can be uncoupled from upstream recruitments under conditions of deregulated RNF168 stability (Gudjonsson *et al*, 2012; Altmeyer & Lukas, 2013a,b). Impaired RNF168 turnover leads to greatly enlarged 53BP1 compartments, which occupy nuclear

territories of several square-micrometers, reaching far beyond the γH2AX/MDC1 domain (Gudjonsson *et al*, 2012). These findings raise the possibility that, despite the hierarchical cascade of DDR factor recruitment, 53BP1 assembly into nuclear compartments may differ from the upstream recruitment of MDC1, and they prompted us to investigate the physicochemical properties of 53BP1 assemblies at sites of DNA lesions and how they affect 53BP1 functions.

Results

Multivalent weak interactions underlying phase separation are sensitive to changes in temperature, salt concentration, pH, and osmotic pressure. In order to assess how DNA repair compartments

would react to changes in osmolarity, we monitored the 53BP1 response to ionizing radiation (IR) by quantitative image-based cytometry (QIBC), a high-content microscopy approach that allows for cell cycle resolved profiling of DNA damage responses (Altmeyer *et al*, 2013; Toledo *et al*, 2013; Ochs *et al*, 2016; Pellegrino *et al*, 2017; Michelena *et al*, 2018). As observed previously, we measured a strong IR-induced increase in nuclear 53BP1 foci in G1, which gradually declined in S-phase when increasing amounts of replicated chromatin promote DSB repair by homologous recombination (Chapman *et al*, 2012; Saredi *et al*, 2016; Pellegrino *et al*, 2017), and which rose again in late G2 (Fig 1A). Consistent with prior work (Giunta *et al*, 2010; Orthwein *et al*, 2014), 53BP1 accumulation was blocked when chromosomes condensed in mitosis (Fig 1B). Sorbitol-induced osmotic stress expectedly resulted in rapid formation of cytoplasmic stress granules (Appendix Fig S1A–C). Strikingly, however, sorbitol addition completely abolished the formation of nuclear 53BP1 compartments at sites of DNA damage (Fig 1C and Appendix Fig S1D). The sorbitol-induced suppression of 53BP1 assembly was comparable to siRNA-mediated depletion of the upstream 53BP1-regulator RNF168 (Appendix Fig S1E and F) and also entailed a complete abrogation of downstream RIF1 assembly at DNA break sites (Fig 1D). Similarly, addition of sucrose or elevated salt concentrations mitigated 53BP1 assembly upon DNA damage (Appendix Fig S2A and B). Live cell experiments using GFP-53BP1 cells confirmed that osmotic stress severely impaired 53BP1 assembly at DNA break sites and also disassembled preformed 53BP1 nuclear bodies at sites of spontaneous DNA lesions (Appendix Fig S2C). We observed very similar effects in non-transformed human epithelial RPE-1 and canine MDCK cells (Appendix Fig S3A and B). The osmotic challenge-induced inhibition of 53BP1 accumulation was fully reversible and was quickly restored when sorbitol was removed after DNA damage induction (Appendix Fig S3C and D). Surprisingly, neither γH2AX nor MDC1 lost their ability to accumulate around DSBs in the presence of osmotic stress, suggesting that the osmosensitivity is specific to the 53BP1 compartment (Fig EV1A and B). Furthermore, 53BP1 assembly, different from γH2AX foci formation, was sensitive to changes in temperature (Fig EV1C and D), and the salt sensitivity was also highly specific for 53BP1 compared to γH2AX (Fig EV1E and F).

While the initial accumulation of γH2AX/MDC1 at sites of DNA damage is essential for the ensuing assembly of 53BP1, MDC1 foci induced by low, sub-lethal doses of IR or neocarzinostatin (NCS) are more transient than 53BP1 foci (Fig 2A and Appendix Fig S4A–D). Indeed, most MDC1 foci had disappeared 2–4 h after damage induction, whereas 53BP1 foci were bright and clearly visible at these later time-points (Fig 2A). Live cell experiments with cells stably expressing either GFP-MDC1 or GFP-53BP1 confirmed the transient nature of MDC1 foci formation and the more long-lived nature of 53BP1 assemblies (Fig 2B). Moreover, and consistent with previous work describing clustering of DNA breaks (Aten *et al*, 2004; Krawczyk *et al*, 2006; Neumaier *et al*, 2012; Roukos *et al*, 2013; Aymard *et al*, 2017; Sollazzo *et al*, 2018), we observed signs of coalescence of 53BP1 compartments over time upon DNA damage (Fig 3A). Comparing 53BP1 and MDC1 foci intensity and area suggested that this was more pronounced for 53BP1 (Fig 3A and B, and Appendix Fig S5A). In time-lapse microscopy experiments, DNA damage-induced 53BP1 compartments showed droplet-like behavior and underwent frequent fusion and occasional fission events

(Fig 3C, and Appendix Fig S5B and C). Moreover, addition of the aliphatic alcohol 1,6-hexanediol, which disrupts weak hydrophobic interactions that are favorable for liquid–liquid phase separation (Molliex *et al*, 2015; Strom *et al*, 2017; Wegmann *et al*, 2018), resulted in disassembly of 53BP1 foci (Appendix Fig S5D and E). Next, in light of the concentration dependency of phase separation and to exclude potential bias from ectopic 53BP1 expression, we employed CRISPR/Cas9 to engineer the endogenous 53BP1 locus and integrate an in-frame sequence encoding for the small monomeric red fluorescent protein mScarlet (Appendix Fig S6A and B). The resulting fusion protein could be visualized by fluorescence microscopy (Appendix Fig S6C), did not affect the cell cycle (Appendix Fig S6D), localized to γH2AX-positive sites of DNA damage (Appendix Fig S6E), showed the typical cell cycle-regulated pattern of 53BP1 accumulation (Appendix Fig S6F), and was sensitive to siRNA treatment targeted against 53BP1 (Appendix Fig S6G). Consistent with our prior results, a short hyperosmotic challenge led to disassembly of 53BP1-mScarlet compartments without affecting γH2AX accumulation (Appendix Fig S6H and I). More importantly, however, live cell experiments with endogenously tagged 53BP1 expressed from its native promoter confirmed the dynamic, droplet-like nature of 53BP1 assemblies, their spherical shape, and their frequent fusions and fissions (Fig 3D and Movie EV1).

Besides clastogen-induced DNA breaks, 53BP1 also assembles at replication stress-induced inherited DNA lesions (Harrigan *et al*, 2011; Lukas *et al*, 2011a). These 53BP1 nuclear bodies, occurring spontaneously and at enhanced frequency upon mild replication stress by low-dose aphidicolin (APH) and ATR inhibitor (ATRi) treatment, showed droplet-like behavior as well, and underwent frequent fusion events (Fig 3E). Finally, and consistent with the transient nature of MDC1 accumulation upon low levels of DNA damage (Fig 2 and Appendix Fig S4), we observed in dual labeling live cell experiments that 53BP1 fusions and fissions typically occurred after discernible foci of MDC1 had disappeared (Appendix Fig S6J). Taken together, we conclude that 53BP1 repair compartments at sites of clastogen-induced DSBs and at heritable DNA lesions show key features of liquid–liquid phase separation.

In order to directly test whether 53BP1 possesses the capacity to phase separate, we turned to a system based on mCherry-labeled *Arabidopsis* photoreceptor cryptochrome 2 (Cry2) fusion proteins to measure target protein optoDroplet formation in living cells (Taslimi *et al*, 2014; Shin *et al*, 2017). As observed before, strong optoDroplet formation occurred for the amino-terminal prion-like domain of FUS, an established model for intracellular phase separation (Shin *et al*, 2017, 2018) and for an oligomerization-prone Cry2 E490G mutant (Taslimi *et al*, 2014), but not for the negative Cry2 wild-type control (Fig EV2A). A Cry2-53BP1 fusion, however, resulted in rapid, light-induced optoDroplet formation (Fig 4A top panel, Fig EV2B for additional examples, and Movie EV2). Introducing a single amino acid exchange (W1495A) within the 53BP1 tandem tudor domain (TTD) to abrogate potentially confounding effects from TTD chromatin and protein interactions (Drane *et al*, 2017), and to assess the intrinsic capacity of 53BP1 to phase separate, further enhanced light-induced optoDroplet formation (Fig 4A middle panel and Movie EV3). Different from 53BP1, Cry2-MDC1 did not show considerable optoDroplet formation (Fig 4A bottom panel and Movie EV4), even though the construct was functional and efficiently accumulated at sites of DNA damage (Fig EV2C). We
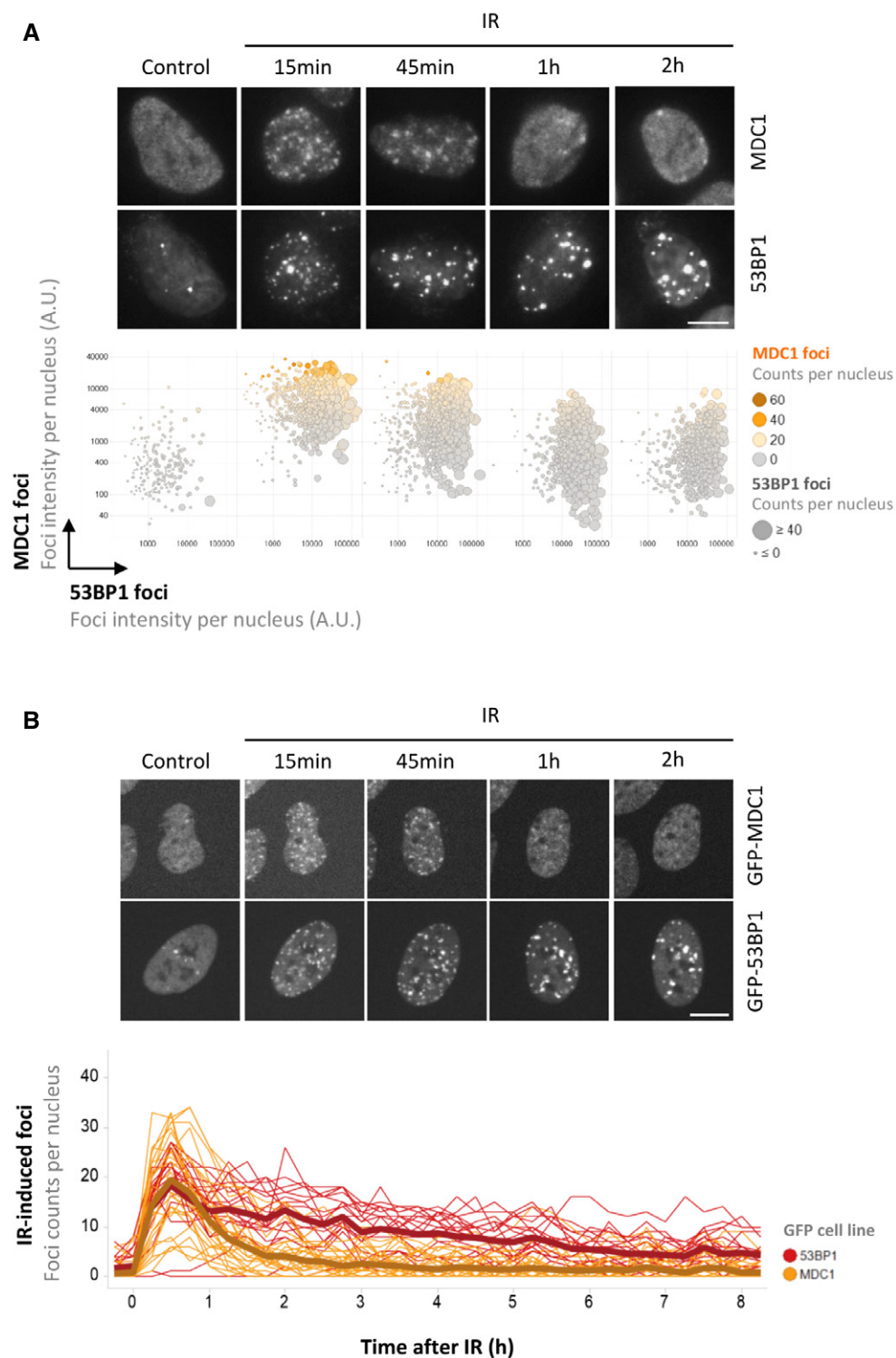
Figure 2. 53BP1 compartments are more long-lived than MDC1 foci.

A U-2 OS cells were treated with 0.5 Gy of IR, allowed to recover for the indicated time periods, stained for 53BP1 and MDC1, and analyzed by QIBC. 53BP1 foci intensities are plotted against MDC1 foci intensities, and representative images are shown.

B U-2 OS cells stably expressing GFP-MDC1 or GFP-53BP1 were treated with 1 Gy of IR and analyzed by live cell microscopy at 15-min intervals. Representative images are provided, and kinetics of GFP-MDC1 and GFP-53BP1 foci formation and dissolution are shown as single-cell tracks. Bold lines represent averages from n = 29 for GFP-MDC1 and n = 18 for GFP-53BP1 cells.
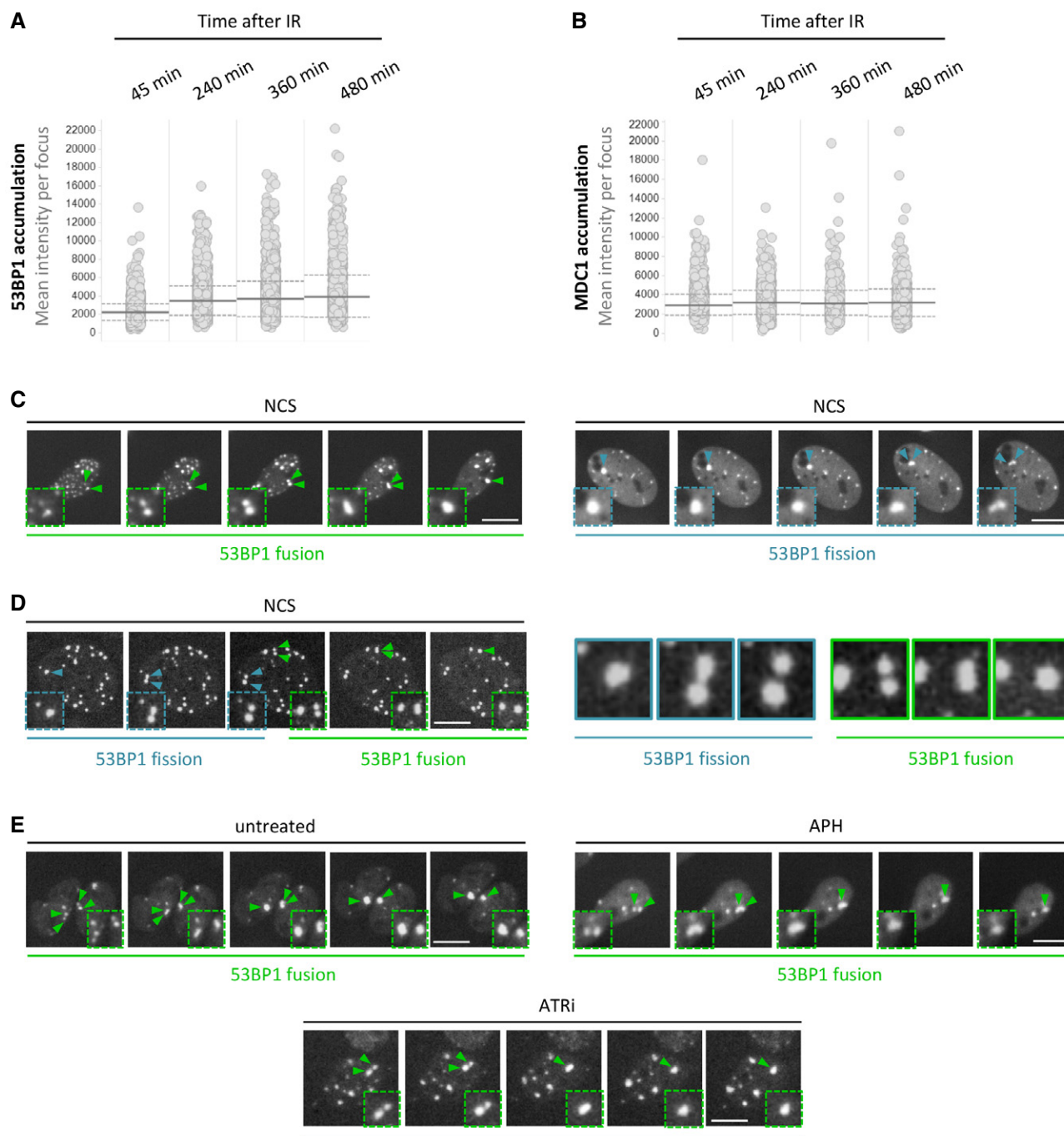
Data information: Scale bars, 10 μm.

Figure 3. 53BP1 repair compartments show droplet-like behavior with fusion and fission events.

A U-2 OS cells were treated with 1 Gy of IR and fixed at the indicated time-points. Mean 53BP1 foci intensity was analyzed from more than 1,500 cells per time-point. Mean (solid line) and standard deviation from the mean (dashed lines) are indicated.

B The same cells as in (A) were analyzed for mean MDC1 foci intensity. Mean (solid line) and standard deviation from the mean (dashed lines) are indicated.

C GFP-53BP1 cells were treated with 25 ng/ml NCS to induce DNA breaks and imaged at 30-min intervals. Examples of GFP-53BP1 fusions (green arrowheads and magnified regions) and fissions (blue arrowheads and magnified regions) are shown.

D 53BP1-RFP cells, in which the endogenous 53BP1 gene locus had been engineered by CRISPR/Cas9 to express 53BP1-mScarlet from the natural promoter, were treated with NCS (25 ng/ml) and imaged at 30-min intervals. Examples of 53BP1 fusions (green arrowheads and magnified regions) and fissions (blue arrowheads and magnified regions) are shown on the left and in higher magnification on the right.

E GFP-53BP1 cells were left untreated, or treated with APH (0.5 μM) or ATRi (1 μM) to induce replication stress-associated heritable DNA lesions, and cells were imaged at 30-min intervals. Examples of 53BP1 fusions (green arrowheads and magnified regions) are shown.
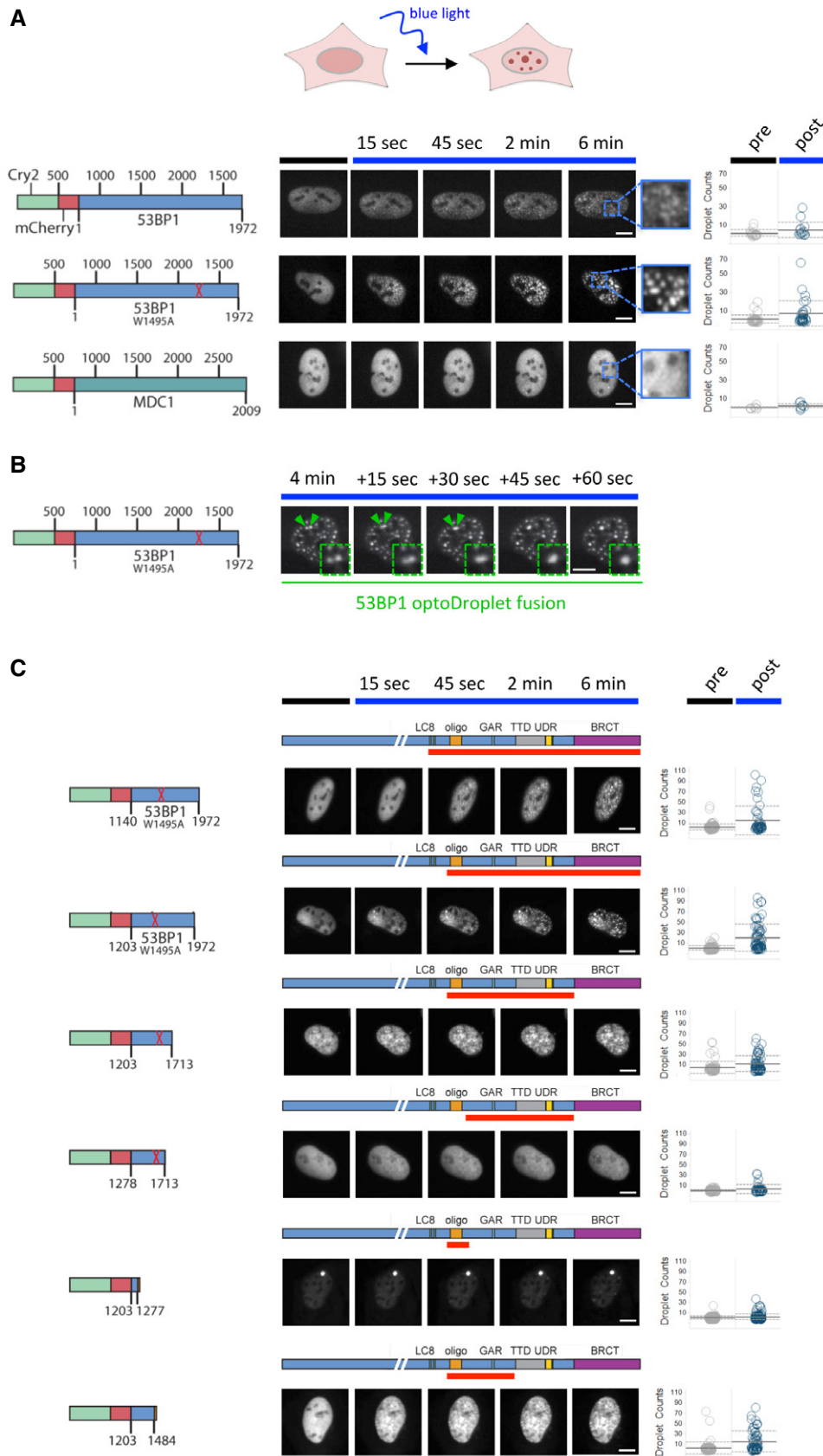
Data information: (C–E) Scale bars, 10 μm.

Figure 4.

Figure 4. 53BP1 phase separates into optoDroplets.

A   Light-induced optoDroplet formation of Cry2-mCherry-53BP1, Cry2-mCherry-53BP1 W1495A, and Cry2-mCherry-MDC1. Cells were imaged at 15-s intervals. Representative images of optoDroplet formation before and 6 min after light induction are shown. Quantifications from single-cell QIBC analysis of 2–3 independent experiments are shown with mean (solid line) and standard deviation from the mean (dashed lines) indicated.

B   Cry2-mCherry-53BP1 W1495A optoDroplet fusion at 15 s time resolution. Fusing optoDroplets are highlighted by green arrowheads and in the magnified insets.

C   Light-induced optoDroplet formation of the indicated Cry2-mCherry-53BP1 constructs. Cells were imaged at 15-s intervals. Representative images and quantifications of optoDroplet formation before and 6 min after light induction are shown. Quantifications from single-cell QIBC analysis of 2–3 independent experiments are shown with mean (solid line) and standard deviation from the mean (dashed lines) indicated. Red bars indicate the part of 53BP1 that was expressed as Cry2-mCherry fusion.

Data information: Scale bars, 10 μm.

noticed that a pH shift from 7.4 to 5.5 rapidly induced FUS optoDroplet formation without light induction (Fig EV2D) and that also 53BP1, but not MDC1, formed optoDroplets under acidic pH (Fig EV2E). Similar to 53BP1 assembly around DNA lesions, 53BP1 optoDroplet fusions could be readily observed, demonstrating their liquid-like behavior (Fig 4B).

Next, we generated a series of deletion mutants to identify the sequence elements driving 53BP1 phase separation. This revealed that the C-terminus, comprising amino acids 1140–1972, was sufficient for optoDroplet formation and that the oligomerization domain (OD) was critically involved (Figs 4C and EV2F). Interestingly, the largely unstructured N-terminus of 53BP1 was dispensable for optoDroplet formation, suggesting that the presence of disordered sequence stretches alone may not be a good predictor for phase separation. Recent work on the FET (FUS, EWSR1, TAF15) protein family identified multivalent interactions between tyrosines (Y) and arginines (R) to promote phase separation (Wang *et al*, 2018). The 53BP1 C-terminus is highly enriched for these amino acids (Appendix Fig S7A), providing a potential explanation for the preferential optoDroplet formation of this region. The OD alone showed strong clustering inside the nucleus yet with abrogated light responsiveness (Fig 4C). When combined with unstructured sequence stretches further toward the C-terminus, however, light-inducible clustering was restored (Figs 4C and EV2F). Surprisingly, we also observed a positive contribution of the C-terminal BRCT domains (Fig 4C), whose function for recruitment and DNA repair by NHEJ has remained ambiguous (Morales *et al*, 2003; Ward *et al*, 2006; Kilkenny *et al*, 2008; Lee *et al*, 2010; Noon *et al*, 2010; Bothmer *et al*, 2011; Lottersberger *et al*, 2013; Knobel *et al*, 2014; Baldock *et al*, 2015; Kleiner *et al*, 2015; Cuella-Martin *et al*, 2016). Multiple sequence elements within the Y/R-rich 53BP1 C-terminus thus seem to cooperate for 53BP1 self-assembly. We focused our further analyses on a construct with the most pronounced light-inducible optoDroplet formation (aa 1203–1972 W1495A). Also with this construct, we observed droplet fusions (Fig 5A), as well as concentration-dependent droplet induction (Fig 5B). In support of the reversibility of 53BP1 assembly, acidic pH-induced optoDroplets were quickly resolved upon buffer exchange back to neutral pH (Appendix Fig S7B) and upon addition of 1,6-hexanediol (Appendix Fig S7C). In fluorescence recovery after photobleaching (FRAP) experiments, individual 53BP1 optoDroplets, 53BP1 nuclear bodies, and IR-induced foci (IRIF) all showed similar recovery kinetics, suggesting a comparable degree of protein mobility (Fig EV3A–D).

In vitro, the purified 53BP1 C-terminus showed condensation into μm-sized droplets in presence of Ficoll (Fig EV4A and B), and 53BP1 condensates co-assembled DSB-mimicking fluorescently

labeled DNA (Fig EV4C and D). *In vivo*, the W1495A construct, despite being impaired in DNA damage recognition when multiple breaks were induced at random genomic regions by NCS (Appendix Fig S8A), accumulated within seconds after light activation at FokI-induced DNA damage at a single genomic region (Fig 5C and Appendix Fig S8B and C), consistent with a seeding-dependent yet self-assembly amplified accrual of 53BP1 to generate the DNA repair compartment. Similar conclusions were recently reached when liquid phase behavior was analyzed by global versus local activation of photo-oligomerizable nucleation centers (Bracha *et al*, 2018).

Our finding that besides the OD also the BRCT domains of 53BP1 contribute to its phase separation was unexpected in light of the ambiguous role of the BRCT domains for 53BP1 recruitment to sites of DNA damage. Of note, however, both the OD and the BRCT domains were recently shown to be required for stabilization of the tumor suppressor p53 and to promote global p53 target gene expression (Cuella-Martin *et al*, 2016). Yet how 53BP1 transmits a local DNA damage signal to promote global p53 activation had remained unclear. Inspired by this conundrum, we revisited the 53BP1/p53 interaction using light-induced optoDroplet formation. While the 53BP1 antagonist BRCA1 showed no significant enrichment in 53BP1 optoDroplets, p53 showed an accumulation in light-induced 53BP1 condensates (Fig 6A). Also, the p53 co-activator USP28 (Cuella-Martin *et al*, 2016; Fong *et al*, 2016; Lambrus *et al*, 2016; Meitinger *et al*, 2016) was enriched in 53BP1 optoDroplets (Appendix Fig S9A), and both p53 and USP28 were found to localize to a fraction of endogenous 53BP1 nuclear bodies (Appendix Fig S9B–D). Enrichment of p53 at DNA break sites was previously observed in ChIP experiments upon cross-linking (Roy *et al*, 2010), and the partial co-localization with 53BP1 nuclear bodies may thus reflect the transient nature of the interaction needed for p53 to exert its gene regulatory functions outside the 53BP1 compartment and/or the oscillatory mode of p53 activation (Reyes *et al*, 2018). We found the assembly of p53 into optoDroplets to be partially dependent on the 53BP1 BRCT domains (Fig 6B), consistent with prior structural and functional studies (Derbyshire *et al*, 2002; Joo *et al*, 2002; Cuella-Martin *et al*, 2016) and, based on our optoDroplet results, indicating that phase-separated 53BP1 compartments might play a role to dynamically assemble and stabilize p53 upon DNA damage. Indeed, when we used sorbitol to disrupt 53BP1 assembly upon DNA damage, without affecting the initial DNA damage recognition and accumulation of γH2AX and MDC1 (Fig EV1), we observed that damage-induced 53BP1/p53 interaction and 53BP1 self-association were impaired (Fig EV5A). Consistently, p53 stabilization after DNA damage was blunted (Figs 6C and EV5B). Moreover, induction of the p53 target gene p21 was abrogated, resulting
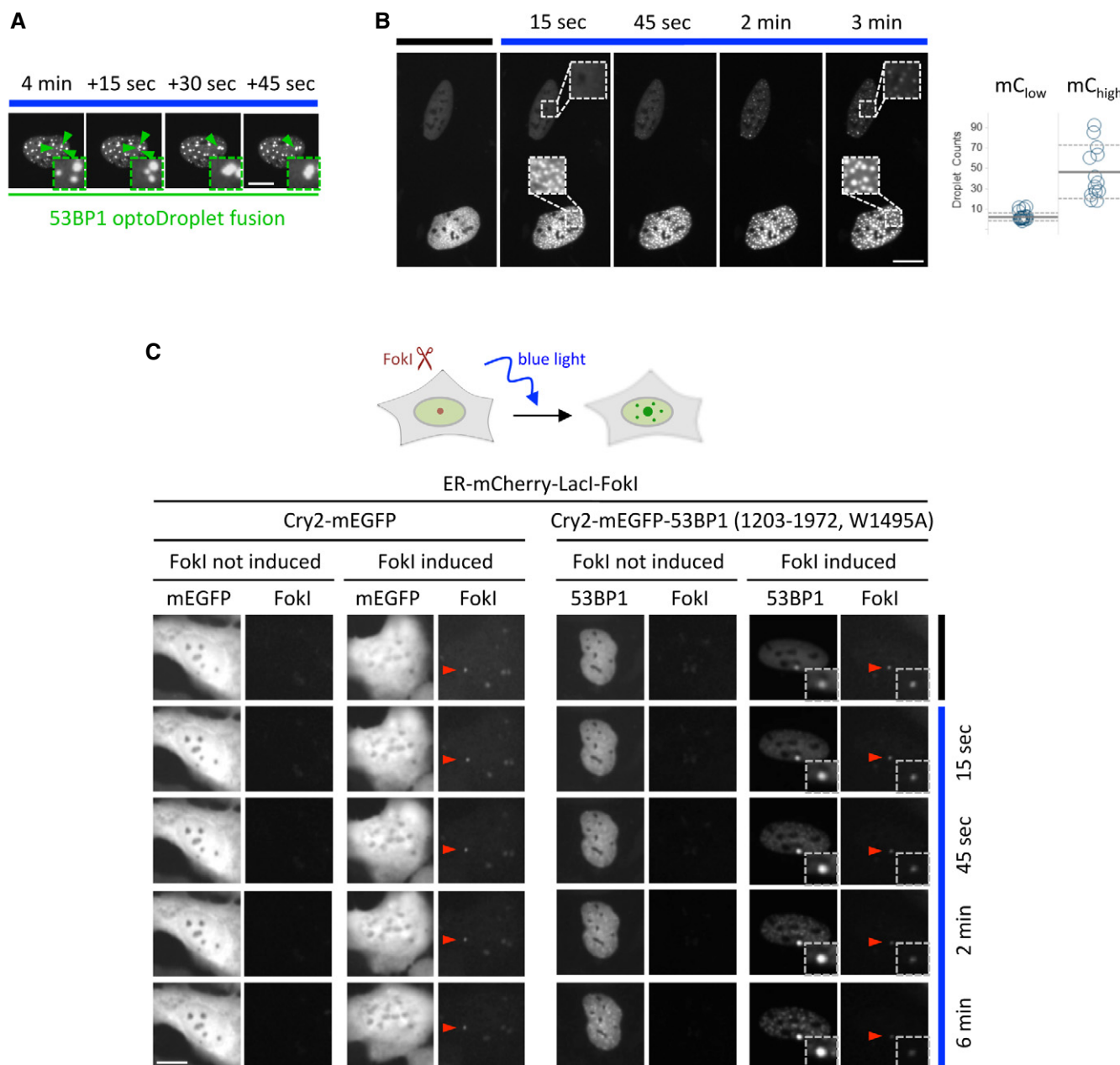
Figure 5. 53BP1 self-assembles at nucleation centers in a concentration-dependent manner.

A Cry2-mCherry-53BP1 1203–1972 W1495A optoDroplets undergo fusion events upon light induction. Fusing optoDroplets are highlighted by green arrowheads and in the magnified insets.

B Concentration-dependent optoDroplet formation exemplified by two neighboring cells that differ in their Cry2-mCherry-53BP1 1203–1972 W1495A expression level. Cells were imaged at 15-s intervals. Quantifications of optoDroplet formation in lowly expressing cells (mC_{low}) and highly expressing cells (mC_{high}) from single-cell QIBC analysis of three independent experiments are shown with mean (solid line) and standard deviation from the mean (dashed lines) indicated.

C Cry2-mEGFP-53BP1 1203–1972 W1495A assembles into FokI-induced DNA repair compartments within seconds after light induction. FokI was induced for 1 h where indicated before cells were light-activated and imaged at 15-s intervals. Red arrowheads mark the FokI-induced lesion with mCherry accumulation.

Data information: Scale bars, 10 μm.

in reduced p21 mRNA (Fig 6D) and protein levels (Fig 6E). In agreement with previous work (Wang *et al*, 2002; Cuella-Martin *et al*, 2016), efficient p53 and p21 induction upon DNA damage was dependent on 53BP1 (Fig EV5C–E). Finally, cell cycle analysis by two-dimensional QIBC based on DNA content (DAPI) and nuclear Cyclin A levels revealed a cell cycle checkpoint defect when 53BP1 assembly and p53 stabilization were blocked by sorbitol (Fig 6F). Accordingly, a checkpoint defect could also be observed in 53BP1-
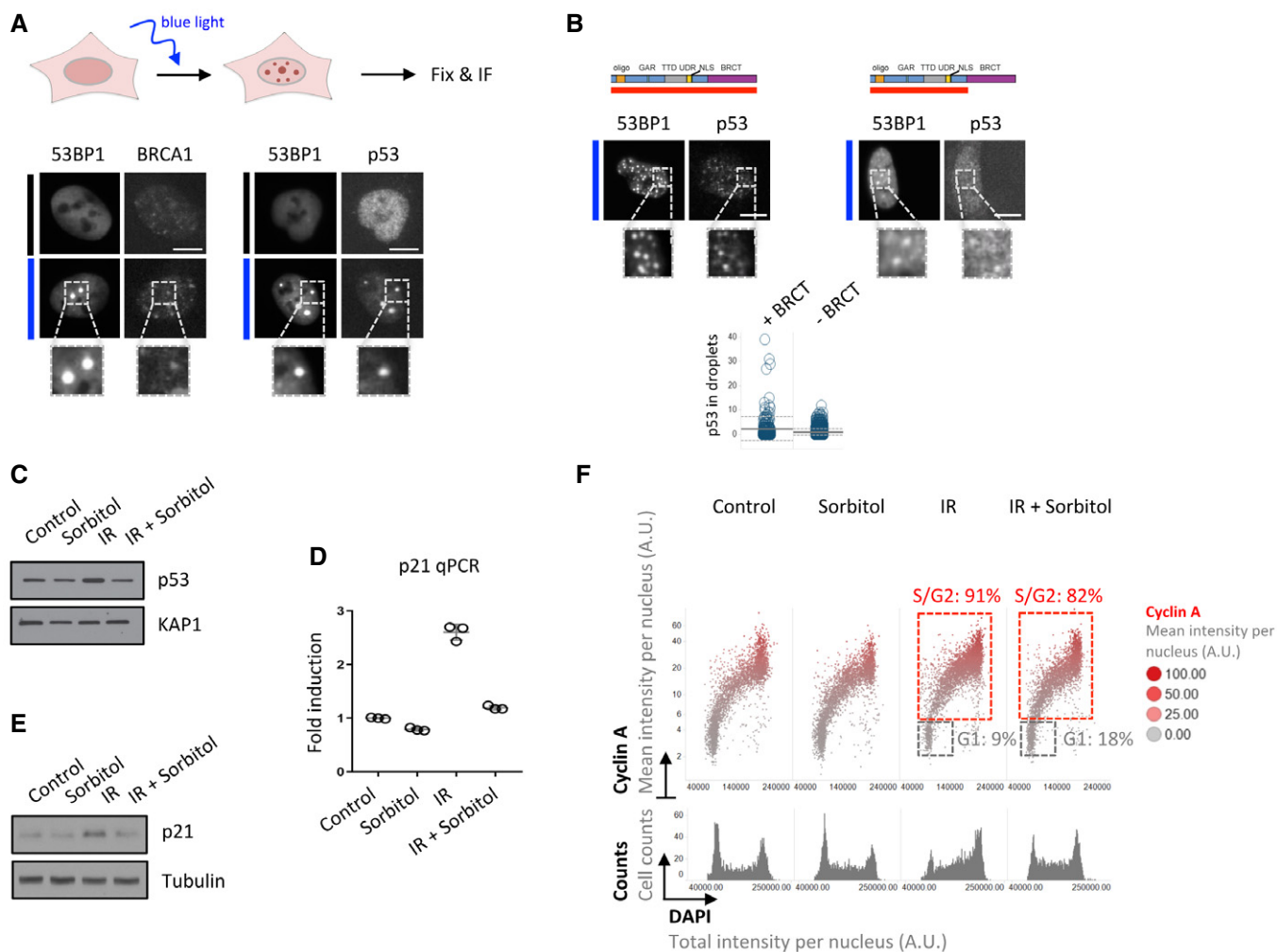
Figure 6. 53BP1 phase separation promotes p53 induction upon DNA damage.

A   Cry2-mCherry-53BP1 1203–1972 W1495A optoDroplets were induced as indicated and fixed 5 min later. Endogenous BRCA1 and p53 were co-stained.
B   As in (A), comparing Cry2-mCherry-53BP1 constructs with and without the BRCT domains. Quantifications of p53 assembly into 53BP1 optoDroplets from single-cell QIBC analysis of 500–600 cells per condition are shown below with mean (solid line) and standard deviation from the mean (dashed lines) indicated. Red bars indicate the part of 53BP1 that was expressed as Cry2-mCherry fusion.
C   Western blot of p53 induction upon DNA damage (10 Gy, 2 h) with and without 0.4 M sorbitol.
D   qPCR of p21 induction upon DNA damage (10 Gy, 2 h) with and without 0.4 M sorbitol. Mean ± standard deviation is indicated.
E   Western blot of p21 induction upon DNA damage (10 Gy, 2 h) with and without 0.4 M sorbitol.
F   QIBC cell cycle analysis based on DNA content and nuclear Cyclin A levels upon DNA damage with and without 0.4 M sorbitol. Cells were irradiated with 2 Gy in absence or presence of 0.4 M sorbitol. After 1 h of recovery, sorbitol-containing medium was exchanged with fresh medium, and cells were allowed to recover for an additional 7 h. Percentages in G1 and S/G2 are provided.

Data information: (A, B) Scale bars, 10 μm.

deficient cells (Fig EV5F), and impaired p53 and p21 induction upon DNA damage was evident upon disruption of 53BP1 assembly by elevated salt concentration or 1,6-hexanediol (Fig EV5G).

Taken together, our results demonstrate that 53BP1 undergoes DNA damage-induced liquid–liquid phase separation (featuring dynamic self-assembly, droplet-like behavior, and frequent fusions of DNA repair compartments) and suggest that 53BP1 phase separation integrates DNA damage detection and shielding of break sites with effector protein activation, including p53 stabilization, thereby coordinating local DNA damage recognition with global alterations in gene expression and checkpoint activation (Figs 7 and EV5H).

Discussion

Previous work had provided first evidence for liquid demixing at sites of DNA damage (Altmeyer *et al*, 2015; Patel *et al*, 2015). Seeded by the DNA damage-induced polyanionic molecule poly (ADP-ribose) (PAR), multiple intrinsically disordered proteins (IDPs), including the FET proteins FUS, EWSR1, and TAF15, transiently assemble at DNA break sites, preceding the accumulation of 53BP1 (Altmeyer *et al*, 2015; Teloni & Altmeyer, 2016). Extended PAR-mediated assembly of IDPs appeared incompatible with concurrent accumulation of 53BP1 (Altmeyer *et al*, 2015),
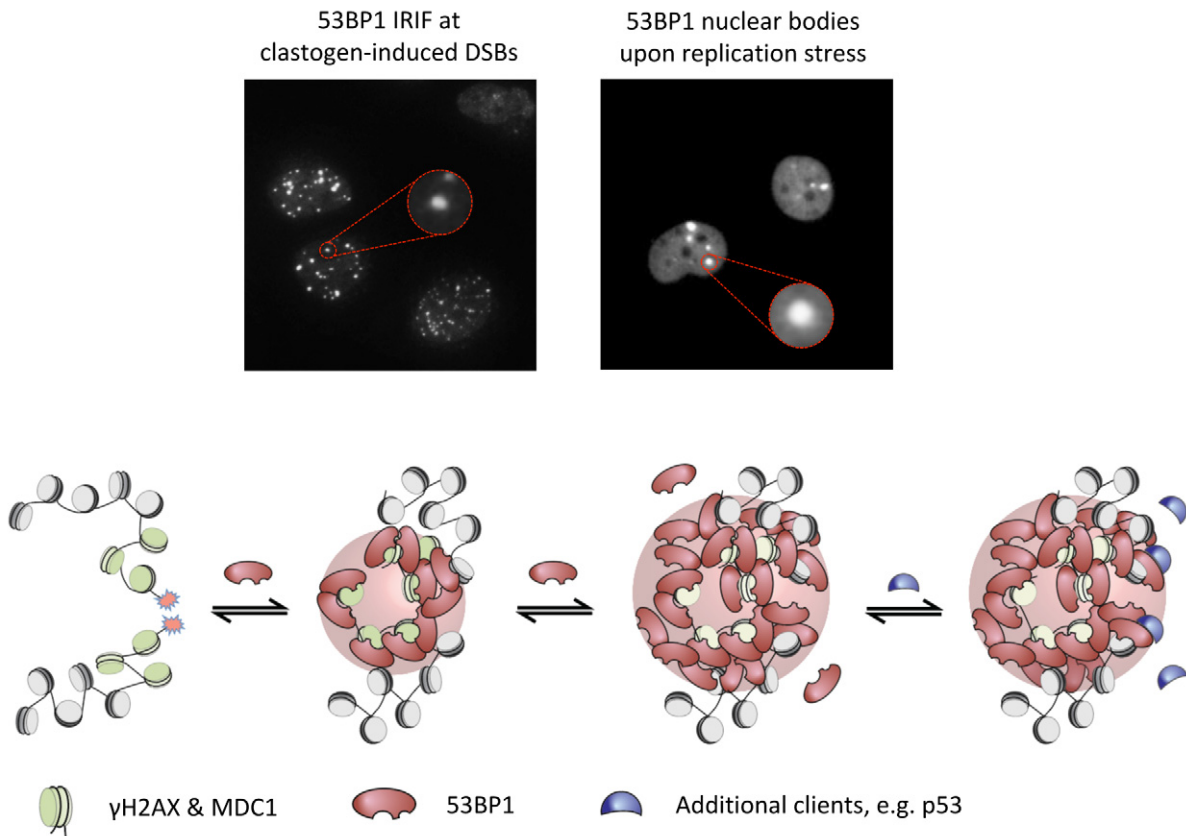
Figure 7. Model of 53BP1 phase separation upon DNA damage.
In accordance with current models on biomolecular condensation and liquid–liquid phase separation (Banani *et al*, 2016; Shin & Brangwynne, 2017; Erdel & Rippe, 2018), upon nucleation by upstream events triggered at sites of DNA damage (γH2AX formation, MDC1 recruitment, activation of RNF8 and RNF168), 53BP1 accumulates and phase separates, acting as scaffold for client molecules such as p53, which transiently interact with the 53BP1 compartment, where they find an environment permissive for their activation. As clients, with lower relative enrichment and higher mobility, they can dissociate again upon activation to carry out effector functions at distant sites in the nucleus. Phase separation of 53BP1 may also promote compartment fusions and clustering of break sites, with potential implications for mis-rejoining of DNA breaks and generation of chromosomal translocations.

suggesting that these two protein assemblages do not intermix well and represent distinct, spatiotemporally separated entities. Once 53BP1 gains access upon termination of the PAR signal, we envision an inner core of 53BP1 assembly in the vicinity of DNA lesions, dependent on cooperative interactions between the TTD and H4K20me2 and between the UDR motif and RNF168-mediated, DNA damage-induced H2AK15 ubiquitin marks, surrounded by an outer layer of 53BP1 assembly via multivalent interactions through the OD and additional disordered sequence stretches within the Y/R-rich C-terminus of 53BP1, including a low complexity glycine/arginine-rich GAR/RGG motif (Thandapani *et al*, 2013) as well as the C-terminal tandem BRCT domain. A somewhat similar multiphase buildup was recently described for sub-compartmentalization of the nucleolus (Feric *et al*, 2016). While the function of the inner core would primarily be to keep broken DNA ends together and protect them from excessive nucleolytic degradation by recruitment of downstream effectors, the outer shell could provide a mechanical buffer zone between repair compartments and undamaged areas of the genome. Along these lines, it was recently demonstrated that phase-separated compartments exert mechanical forces that can rearrange chromatin (Shin *et al*, 2018), and it is tempting to

speculate that 53BP1 condensation might push undamaged chromatin regions away from break sites, and organize damaged chromatin into larger repair compartments. While such repair centers may be beneficial to concentrate repair enzymes and exclude interfering protein machineries, clustering of multiple break sites in close proximity within a single compartment comes with the risk of promoting chromosomal translocations. Indeed, 53BP1 promotes telomere fusions and mis-rejoining of DSBs in BRCA1-deficient cells (Bunting *et al*, 2010; Lottersberger *et al*, 2015). Further studies will be needed to elucidate how cells balance the benefits and risks of generating large phase-separated compartments around DNA break sites and to link 53BP1 droplet fusion and fission events with repair outcome. Upon growth of the 53BP1 compartment around DNA break sites, the enlarged surface area will increase the chances for signaling molecules such as p53 to become activated in a DNA damage-dependent manner, yet without having to directly interact with the broken DNA ends or with the molecular machinery involved in DSB repair. Of note, such 53BP1-mediated p53 stabilization might even persist after the homologous recombination (HR) factor BRCA1 has displaced 53BP1 from the inner core to the outer shell in S/G2 cells to initiate HR (Chapman *et al*, 2012), and is in

line with p53 being detected in APEX-based proximity labeling of 53BP1, but not of BRCA1 or MDC1 (Gupta *et al*, 2018). The gradual dilution of DSB-induced chromatin modifications away from the break site would thus establish functional divergence within the 53BP1 domain, with direct chromatin interactions governing the initial 53BP1 recruitment, and 53BP1 self-assembly-driven interactions toward the periphery. Such a multiphase buildup may reconcile why certain sequence domains of 53BP1 play controversial roles in 53BP1 foci formation, yet are required for transmitting the DNA damage signal to the cell cycle checkpoint machinery. In accordance, we found that the W1495A TTD mutation abolished foci formation when multiple DNA lesions were induced, but allowed for damage recruitment when a strong singular nucleation event was provided by FokI induction (Appendix Fig S8B and C). Such findings highlight the need to consider the number of nucleation centers, i.e., DNA break sites, that are present at any given point in time, and provide a theoretical framework to revisit seemingly conflicting results on the contribution of individual 53BP1 protein domains for its damage-induced assembly.

Finally, while the critical role of the 53BP1 OD for microscopically discernible foci formation is difficult to reconcile with stoichiometric recruitment to RNF168-ubiquitylated histones, this requirement can be rationalized by a self-assembly process that allows the 53BP1 compartment to grow beyond the initial seed site, in particular when the number of nucleation centers is low. Such an expanded layer of the 53BP1 scaffold can function as reaction hub to transiently assemble client molecules, including p53 and p53-activatory proteins, and to relay the signal from locally confined repair compartments to global activation of p53 target genes to control checkpoint functions and regulate cell fate decisions.

Materials and Methods

Cell culture

Human U-2 OS cells (authenticated by STR profiling), U-2 OS derived stable cell lines expressing GFP-53BP1, GFP-MDC1, or 53BP1-mScarlet, U-2 OS cells harboring an array of the lac operator sequence and stably expressing ER-mCherry-LacI-FokI (Tang *et al*, 2013), hTERT-RPE1 cells, MCF7 wild-type, MCF7 53BP1 knockout, and canine MDCK cells were grown under standard sterile cell culture conditions (37°C, humidified atmosphere, 5% CO_2) in Dulbecco's modified Eagle's medium (DMEM, Thermo Fisher) containing 10% fetal bovine serum (GIBCO) and penicillin–streptomycin antibiotics. All cell lines were routinely tested for mycoplasma contamination by PCR and scored negative. FokI in ER-mCherry-LacI-FokI cells was induced with 300 nM 4-OHT (Sigma-Aldrich) and 1 μM Shield (Takara) for 1–2 h. Sorbitol, sucrose, sodium chloride (NaCl), and 1,6-hexanediol (all from Sigma-Aldrich) were prepared freshly in DMEM prior to cell treatments. Neocarzinostatin (NCS) and aphidicolin were from Sigma-Aldrich; the ATR inhibitor AZ-20 was from Tocris.

Cloning

Cloning was done using chemically competent bacteria generated in-house, derived from Library Efficiency™ DH5α™ Competent Cells (ThermoFisher). Correct cloning and integration into target vectors were confirmed by sequencing.

Cloning of components for endogenous 53BP1 tagging

The mScarlet-P2A-NeoR construct was generated from three-piece Gibson assembly. The pUC18 vector was generated by linearization with primers 1 and 2. The mScarlet gene was initially amplified from the pmScarlet-i_C1 plasmid (Bindels *et al*, 2017; Addgene 85044) with primers 6 and 7 followed by amplification of the product with primers 5 and 7. The Neo resistance gene was amplified from the same plasmid with primers 3 and 4. After Gibson assembly of these components, the product was transformed and plasmids isolated and verified by sequencing. pX459 targeting the C-terminal of 53BP1 was generated as previously described (Ran *et al*, 2013) by T4 PNK (NEB)-mediated phosphorylation and annealing of primers 10 and 11 at 10 μM. The product was diluted and assembled into the vector by golden gate assembly using BBsI (NEB) and T4 DNA ligase (NEB) through 12 cycles between 5 min at 37°C and 5 min at 16°C followed by transformation and isolation of plasmids to identify the correct product. The repair template for tagging of endogenous 53BP1 by homology-directed repair was amplified by PCR of the mScarlet-NeoR pUC18 plasmid generated above, using Q5 (NEB) polymerase amplification with primers 8 and 9 followed by PCR purification with a QIAquick PCR purification column according to the manufacturer's instruction.

Cloning of Cry2-mCherry-fusion constructs

The E490G mutation in Cry2olig-mCherry (Taslimi *et al*, 2014) (Addgene 60032) was reverted with primers 14 and 15 using Q5 site-directed mutagenesis to generate Cry2WT-mCherry. To generate a W1495A TTD mutant of 53BP1, N-Myc-53BP1 pLPC-Puro (Dimitrova *et al*, 2008; Addgene 19836) was mutated using Q5 site-directed mutagenesis with primers 12 and 13. The Cry2WT-mCherry-53BP1 fusion constructs were generated by Gibson assembly of the desired 53BP1 fragments into the Cry2WT-mCherry vector linearized with primers 16 and 17. Full-length and truncated versions of 53BP1 were generated by amplification of the desired insert with forward and reverse primer sets from the primer list (18 + 19, 24–33) or by Q5 site-directed deletion from already cloned products with primers 34–37. The products were DpnI digested and gel extraction purified followed by isothermal Gibson assembly into the linearized vector and transformation into competent DH5α. The N terminus of FUS and MDC1 was similarly amplified with primer sets 20 + 21 and 22 + 23, respectively, followed by Gibson assembly into the linearized vector. Exchange of the mCherry fluorescent protein with mEGFP in the Cry2 constructs was performed by PCR amplification on the Cry2WT-mCherry empty vector with primers 16 + 38 and on the corresponding Cry2WT-mCherry-53BP1(1203–1972) vector with primers 16 + 27, followed by inserting mEGFP (Addgene 18696) amplified with primers 39 + 40 or 39 + 41 by Gibson assembly into the linearized backbones.

Cloning of MDC1-mScarlet

The mScarlet-i-C vector was linearized by Q5 polymerase amplification with primers 42 + 43, and MDC1 was amplified from the GFP-MDC1 construct with Q5 polymerase with primers 44 + 45 followed by insertion by Gibson assembly into the linearized vector.

Cloning of GST-tagged mCherry-53BP1 (1203–1972) and 53BP1 (1203–1972)

pGEX6 was linearized with primers 46 and 47 followed by DpnI digestion and gel extraction purification. The inserts harboring parts of 53BP1 with or without mCherry were amplified with primers 48–50 followed by DpnI digestion and gel extraction purification. The inserts were cloned into the vector by isothermal Gibson assembly and the products transformed into DH5α.

Engineering of the endogenous 53BP1 locus

400,000 U-2 OS cells were seeded into wells of a 6-well plate 1 day before transfection. 1 μg of the repair template and 1 μg of the 53BP1 targeting pX459 were diluted in 250 μl OptiMEM (Thermo Fisher) and prepared for transfection with 6 μl TransIT-LT1 (Mirus Bio) followed by 15 min incubation. The same transfection mix was prepared without the repair template as control. The transfection mixtures were added to the cells at a confluence of 80–90%. On the next day, the cells were transferred to 16-cm plates. Selection was initiated 2 days after transfection by incubation with 400 μg/ml G418 (Thermo Fisher). Medium was exchanged every 3–4 days for the next 20–25 days until colonies were obtained and when clear signs of cell death were observed for the cells transfected without repair template. Individual clones were picked by trypsin detachment in cloning cylinders and transferred to a 24-well plate for subsequent expansion for the next 10 days under continued selection. Cells were then transferred to 6-well plates, expanded further, and characterized by QIBC for expression and functionality and by PCR-based analysis of genomic DNA to confirm the correct insertion of the mScarlet-P2A-NeoR module with primers 51 and 52.

Fluorescence and brightfield microscopy

GE IN Cell Analyzer 2500HS

IN Cell Analyzer 2500HS was equipped with two filter sets for multi-wavelength acquisitions: BGOFR_1, blue (ex BP 390/18, em BP 432/47), green (ex BP 475/28, em BP 511/23), orange (ex BP 542/27, BP 587/48), and far-red (ex BP 632/22, em BP 676/48), and BGFFR_2, blue (ex BP 390/18, em BP 432/47), green (ex BP 475/28, em BP 526/52), red (ex BP 575/25, BP 607/19), and far-red (ex BP 632/22, em BP 676/48). The associated objectives used were a 20× NA 0.75 CFI Plan Apo lambda and a 40× NA 0.95 CFI Plan Apo lambda objective. Images were acquired with a 16-bit 2,048 × 2,048 pixel PCO sCMOS camera with a pixel size of 6.5 μm.

Olympus ScanR

The Olympus ScanR imaging system based on an inverted motorized Olympus IX83 microscope was equipped with one set of bandpass filters for multi-wavelength acquisition: DAPI (ex BP 395/25, em BP 435/26), FITC (ex BP 470/24, em BP 511/23), TRITC (ex BP 550/15, BP 595/40) and Cy5 (ex BP 640/30, em BP 705/72). The associated objectives used were a 20× NA 0.75 UPLSAPO and a 40× NA 0.90 UPLSAPO air objective. Images were acquired with 12-bit dynamics on a 16-bit 2,048 × 2,048 pixel Hamamatsu ORCA-FLASH 4.0 V2 sCMOS camera with pixel size of 6.5 μm.

Molecular devices IXM-C

The IXM-C system used for spinning disk confocal imaging was equipped with bandpass filters for multi-wavelength acquisition: DAPI (ex BP 377/25, em BP 447/30), FITC (ex BP 480/15, em BP 535/20), TRITC (ex BP 542.5/7.5, BP 642.5/32.5), Texas Red (ex BP 560/20, BP 630/30) and Cy5 (ex BP 624/20, em BP 692/20), and with lasers at 405, 488, 532, and 633 nm. The objectives used were a 20× NA 0.75 Apo lambda and a 40× NA 0.95 Plan Apo Lambda air objective. Images were acquired with a 16-bit 2,048 × 2,048 pixel Andor sCMOS camera with pixel size of 6.5 μm.

Leica SP5 UV-VIS

The Leica SP5 was equipped with an Argon laser for 453, 476, 488, 496, and 514 nm, and a diode laser for 561 nm. The filters for fluorescence imaging were GFP (ex BP 470/40, em BP 525/50) and N3 (ex BP 546/12, 600/400). Confocal images were acquired with an HCX PL APO Leica 63× oil immersion objective with PMT detectors.

EVOS Floid Cell Imaging Station

An EVOS Floid Cell Imaging Station allowed for transmission light and fluorescence imaging with filters for blue (ex BP 390/40, em BP 446/33), green (ex BP 482/18, em BP 532/59), and red (ex BP 586/15, em BP 646/68). The system was equipped with a 20× NA 0.45 Plan Fluorite air objective and a digital camera for acquisition with 1,296 × 964 pixel resolution.

Micrographs are displayed with adjusted brightness and contrast settings, with identical settings being used to compare conditions within the same experiment.

Immunostaining

Cells were grown in imaging multi-well plates or on sterile 12-mm glass coverslips, fixed in 3% formaldehyde in PBS for 15 min at room temperature, washed once in PBS, permeabilized for 5 min at room temperature in PBS supplemented with 0.2% Triton X-100 (Sigma-Aldrich), and washed twice in PBS. All primary (detailed below) and secondary antibodies (Alexa Fluor 488, 568, and 647 anti-rabbit and anti-mouse IgGs from Thermo Fisher) were diluted in filtered DMEM containing 10% FBS and 0.02% sodium azide. Antibody incubations were performed for 1–2 h at room temperature. Following antibody incubations, cells were washed once with PBS and incubated for 10 min with PBS containing 4',6-diamidino-2-phenylindole dihydrochloride (DAPI, 0.5 μg/ml) at room temperature to stain DNA. Following three washing steps in PBS, cells in multi-well plates were kept in PBS for the imaging, whereas cells on coverslips were briefly washed with distilled water and mounted on glass slides with 5 μl Mowiol-based mounting media (Mowiol 4.88 (Calbiochem) in Glycerol/TRIS).

Quantitative image-based cytometry (QIBC)

Automated multichannel wide-field microscopy for quantitative image-based cytometry (QIBC) was performed on the Olympus ScanR Screening System described above as done previously (Pellegrino *et al*, 2017; Lezaja & Altmeyer, 2018; Michelena *et al*, 2018). Images were analyzed with the Olympus ScanR Image Analysis Software version 3.0.0, a dynamic background

correction was applied, nuclei segmentation was performed using an integrated intensity-based object detection module using the DAPI signal, and foci segmentation was performed using an integrated spot-detection module. All downstream analyses were focused on properly detected interphase nuclei containing a 2C–4C DNA content as measured by total and mean DAPI intensities. Fluorescence intensities were quantified and are depicted as arbitrary units. Color-coded scatter plots of asynchronous cell populations were generated with Spotfire data visualization software version 7.0.1 (TIBCO). Within one experiment, similar cell numbers were compared for the different conditions. For visualizing discrete data in scatter plots, mild jittering (random displacement of data points along the discrete data axes) was applied in order to demerge overlapping data points. Representative scatter plots, typically containing several thousand cells each, are shown. Corresponding images, in which individual color channels have been adjusted for brightness and contrast, accompany selected quantifications.

Live cell tracking of foci formation in GFP-MDC1 and GFP-53BP1 U-2 OS cells

Live imaging of U-2 OS cells in 96-well ibidi plates was carried out on the GE InCell microscope described above with controlled atmosphere (5% CO_2 and 20% O_2) and temperature (37°C). Images were acquired every 15 min with 100 ms exposure. After 30 min, the plate was exposed to 1 Gy of ionizing radiation and returned for imaging the next 8 h. Image stacks were converted and imported to Olympus ScanR Image Analysis Software version 3.0.0. Nuclei segmentation was done on smoothened GFP signal to avoid mis-segmentation upon foci formation and foci detection was carried out with the spot-detection module described above. Result tables were extracted to include frame numbers and x-y coordinates of the center of the nuclei. These coordinates were used as a basis for a script to track cells based on closest proximity in x-y pixel space between consecutive frames (MATLAB code at https://github.com/SinKilic/Tracking), and the associated time-dependent development of foci counts was visualized in Spotfire.

Fluorescence recovery after photobleaching

Fluorescence recovery after photobleaching was carried out on the Leica SP5 system described above. Bleaching movies were acquired with photon collection in 128 × 128 pixels at a zoom of 28 with a speed of 700 Hz and a pinhole set at 210 μm. The argon laser was turned on to 100%, and images during FRAP were acquired with the 488 nm laser line at a laser power of 10%, an EV gain of 750 and the PMT detection range set to 495–580 nm for GFP acquisitions and to 585–640 nm for mCherry acquisitions (565 nm laser). The time to acquire per frame was 389 ms. Five images were acquired prior to bleaching a circular area with 1 μm diameter using 100% laser power for five cycles, followed 60 images to monitor the recovery. Signals were corrected for photobleaching using a similarly sized unbleached area and then normalizing to the ratio between the average intensity of the 5-prebleach images and the lowest post-bleach intensity. Averages ± standard deviation from 12 to 20 cells per condition were plotted.

Cry2 light-mediated phase separation

Two days prior to microscopy, 6,000 U-2 OS or 8,000 U-2 OS cells harboring the lac operator array and stably expressing ER-mCherry-LacI-FokI were seeded into a 96-well plate (Greiner μclear). Twenty-four hours prior to microscopy, cells were transfected with 100 ng plasmid DNA per well using TransIT-LT1. The DNA was diluted in 9 μl OptiMEM per transfection, 0.3 μl LT1 was added, and the mixture was incubated for 15 min at room temperature. The transfection mix was diluted in 92 μl FluoroBrite DMEM supplemented with Glutamax and FCS and added to the cells. Microscopy of optoDroplet formation was carried out using the IN Cell Analyzer 2500HS system. Acquisitions were done with the 20× objective using the BGRFR_2 filter set with 100 ms red exposures for visualization of the mCherry signal and 25 ms green2 exposures for Cry2 activation. For mEGFP-tagged versions, 100 ms green2 exposures were used for light activation and detection of the mEGFP-tagged proteins. Time-lapse image sequences were obtained with 15-s interval acquisitions with green2 exposure after each red exposure for 6 min. OptoDroplet quantification was performed on unprocessed images using the Olympus ScanR Image Analysis software and the integrated spot-detection module. Cells with similar expression levels were compared.

Live cell imaging of 53BP1 fusions and fissions

Fusions and fissions of 53BP1 using GFP-53BP1 U-2 OS cells were observed with 2-min intervals in spinning disk confocal mode on the IXM-C system and with 30-min intervals on the ScanR system. 53BP1 fusions and fissions using genetically engineered endogenously tagged 53BP1-mScarlet cells were observed on the In Cell 2500HS imaging system. Images were continuously acquired for up to 2 h with 2-min intervals or 24 h with 30-min intervals. Image stacks were generated and processed with Fiji (ImageJ).

Expression and purification of recombinant 53BP1 1203–1972

Expression of recombinant proteins was performed in BL21 (DE3) cells from pGEX-6P-1 plasmids harboring 53BP1 W1495A (1203–1972) or mCherry-53BP1 W1495A (1203–1972). 4 ml from a bacterial pre-culture grown from a single colony was inoculated into 400 ml LB medium with 100 μg/ml ampicillin (Sigma-Aldrich) and grown at 30°C and 230 rpm until reaching an OD600 of 0.6. The temperature was then lowered to 16°C, and expression was induced with IPTG at a final concentration of 0.2 mM followed by 16 h of expression. Bacteria were harvested by centrifugation at 5,000 g for 20 min and resuspended in 20 ml binding buffer (50 mM Tris pH 7.4, 200 mM NaCl, 0.05% NP-40, 1 mM EDTA, 1 mM DTT, 10% glycerol, 1 mM PMSF, pepstatin, bestatin, and leupeptin 1 μg/ml each) followed by cell lysis by two passages through a French press. The supernatant was recovered by centrifugation at 25,000 g for 30 min. The supernatant was loaded onto a pre-equilibrated 1 ml GSTrap FF (GE Healthcare Life Sciences) and washed with 10 column volumes of binding buffer. Bound proteins were eluted with 10 column volumes of elution buffer (50 mM Tris pH 7.4, 150 mM NaCl, 0.05% NP-40, 1 mM EDTA, 1 mM DTT, 10% glycerol, 40 mM glutathione, and 1 tablet cOmplete protease inhibitor tablet (Roche) per 50 ml buffer). Eluted

fractions were analyzed by 10% SDS–PAGE. 50 µl glutathione sepharose 4B beads (GE Healthcare Life Sciences) pre-equilibrated with binding buffer at 4°C and diluted fractions from the initial purification were mixed to allow binding for 2 h. After binding, the beads were collected by centrifugation and washed three times with 1 ml binding buffer. Beads were then washed three times with 1 ml PBS containing 1 mM DTT and incubated with 50 µl PBS containing 1 mM DTT and 20 µg PreScission protease. Cleaved proteins were recovered from the supernatant by centrifugation, and the protein concentration was determined by Bradford assay.

In vitro 53BP1 condensation

A mix of 53BP1 W1495A (1203–1972) and mCherry-53BP1 W1495A (1203–1972; 9:1 ratio) was diluted with Ficoll 400 (Sigma-Aldrich) to a final concentration of 1.66 µM protein, 12.5% Ficoll with or without 125 nM FAM-labeled dsDNA (primers 53 and 54) in 20 µl. The mixtures were transferred to a 384-well plate and analyzed on the Floid Imaging system and on the Leica SP5 UV-VIS confocal system equipped for simultaneous brightfield and fluorescence imaging.

siRNA transfections

Individual siRNA transfections were performed for 72 h with Ambion Silencer Select siRNAs using Lipofectamine RNAiMAX (Thermo Fisher) according to the manufacturer's procedures. The following Silencer Select siRNAs were used: siControl, s813; siRNF168, s46600; si53BP1, s14313; sip53, s606; siUSP28, s33509.

Irradiation of cells

Irradiation was performed with a Faxitron Cabinet X-ray System Model RX-650 at IR doses from 0.5 to 10 Gy.

RNA extraction, reverse transcription, and quantitative PCR

RNA was purified with TRIzol reagent (Life Technologies), primed with random hexamers (11034731001, Roche), and reverse-transcribed using MultiScribe Reverse Transcriptase (4311235, Thermo Fisher). Quantitative PCR (qPCR) was performed with the KAPA SYBR FAST qPCR Kit (KAPA Biosystems) on a Rotor-Gene Q system (Qiagen). Relative transcription levels were obtained by normalization to EIF2C2, RPS12, and GAPDH expression. At least two biological experiments were conducted with qPCRs performed in triplicates. Primers 55–62 were used for amplification.

Co-immunoprecipitation

U-2 OS GFP-53BP1 grown in a 10-cm plate was transfected with 5 µg N-Myc-53BP1 WT pLPC-Puro using Lipofectamine 3000. Twenty-four hours post-transfection cells were treated with IR (10 Gy) in presence or absence of 0.4 M sorbitol and allowed to recover for 2 h. Cells were washed with PBS and directly lysed with 500 µl of TNE buffer (50 mM Tris–HCl pH 8.0, 150 mM NaCl, 0.1% Igepal CA630 (NP-40), 1 mM EDTA, 2 mM MgCl$_2$, complete inhibitor cocktail (Roche), phosphoSTOP (Roche), and 25 U/ml benzonase). Lysates were incubated for 5 min at room temperature and then centrifuged at 15,000 g for 15 min. 500 µg of lysates was

incubated with protein G-sepharose (15 µl slurry) coupled with 1 µl of anti-GFP antibody for 3 h at 4°C. Beads were collected by centrifugation, washed four times with lysis buffer, and eluted by boiling in 10× SDS–PAGE sample buffer. Samples were then run on a 7.5% SDS–PAGE for immunoblotting.

Immunoblotting

Proteins were separated by SDS–PAGE and transferred onto PVDF membranes. Membranes were blocked with 5% milk in PBS-T (PBS + 0.1% Tween-20) for 1 h at room temperature and incubated with primary antibodies overnight at 4°C. Membranes were then washed three times with PBS-T and incubated with HRP-conjugated secondary antibodies for 1 h at room temperature, washed again three times with PBS-T, and protein signals were detected using ECL™ Western Blotting Detection Reagent (Amersham™).

Data availability

All source data, including high-content imaging data for QIBC analysis, are stored on a secure UZH server and can be made available upon request. Original Western blot scans have been uploaded to Mendeley.

Expanded View for this article is available online.

Author contributions
Methodology, investigation, data curation, visualization: SK, AL, MG, JM, EB, RI, MA; conceptualization: MA and SK; project design, supervision, administration and funding acquisition: MA; manuscript writing: MA with help from SK; reviewing and editing: SK, AL, MG, JM, EB, RI, MA.

Conflict of interest
The authors declare that they have no conflict of interest.

References

Aguzzi A, Altmeyer M (2016) Phase separation: linking cellular compartmentalization to disease. *Trends Cell Biol* 26: 547–558

Alberti S (2017) Phase separation in biology. *Curr Biol* 27: R1097–R1102

Altmeyer M, Lukas J (2013a) Guarding against collateral damage during chromatin transactions. *Cell* 153: 1431–1434

Altmeyer M, Lukas J (2013b) To spread or not to spread—chromatin modifications in response to DNA damage. *Curr Opin Genet Dev* 23: 156–165

Altmeyer M, Toledo L, Gudjonsson T, Grofte M, Rask MB, Lukas C, Akimov V, Blagoev B, Bartek J, Lukas J (2013) The chromatin scaffold protein SAFB1 renders chromatin permissive for DNA damage signaling. *Mol Cell* 52: 206–220

Altmeyer M, Neelsen KJ, Teloni F, Pozdnyakova I, Pellegrino S, Grofte M, Rask MBD, Streicher W, Jungmichel S, Nielsen ML *et al* (2015) Liquid demixing of intrinsically disordered proteins is seeded by poly(ADP-ribose). *Nat Commun* 6: 8088

Aten JA, Stap J, Krawczyk PM, van Oven CH, Hoebe RA, Essers J, Kanaar R (2004) Dynamics of DNA double-strand breaks revealed by clustering of damaged chromosome domains. *Science* 303: 92–95

Aymard F, Aguirrebengoa M, Guillou E, Javierre BM, Bugler B, Arnould C, Rocher V, Iacovoni JS, Biernacka A, Skrzypczak M *et al* (2017) Genome-wide mapping of long-range contacts unveils clustering of DNA double-strand breaks at damaged active genes. *Nat Struct Mol Biol* 24: 353–361

Baldock RA, Day M, Wilkinson OJ, Cloney R, Jeggo PA, Oliver AW, Watts FZ, Pearl LH (2015) ATM localization and heterochromatin repair depend on direct interaction of the 53BP1-BRCT2 domain with gammaH2AX. *Cell Rep* 13: 2081–2089

Banani SF, Rice AM, Peeples WB, Lin Y, Jain S, Parker R, Rosen MK (2016) Compositional control of phase-separated cellular bodies. *Cell* 166: 651–663

Banani SF, Lee HO, Hyman AA, Rosen MK (2017) Biomolecular condensates: organizers of cellular biochemistry. *Nat Rev Mol Cell Bio* 18: 285–298

Bindels DS, Haarbosch L, van Weeren L, Postma M, Wiese KE, Mastop M, Aumonier S, Gotthard G, Royant A, Hink MA *et al* (2017) mScarlet: a bright monomeric red fluorescent protein for cellular imaging. *Nat Methods* 14: 53–56

Blackford AN, Jackson SP (2017) ATM, ATR, and DNA-PK: the trinity at the heart of the DNA damage response. *Mol Cell* 66: 801–817

Boehning M, Dugast-Darzacq C, Rankovic M, Hansen AS, Yu T, Marie-Nelly H, McSwiggen DT, Kokic G, Dailey GM, Cramer P *et al* (2018) RNA polymerase II clustering through carboxy-terminal domain phase separation. *Nat Struct Mol Biol* 25: 833–840

Boeynaems S, Alberti S, Fawzi NL, Mittag T, Polymenidou M, Rousseau F, Schymkowitz J, Shorter J, Wolozin B, Van Den Bosch L *et al* (2018) Protein phase separation: a new phase in cell biology. *Trends Cell Biol* 28: 420–435

Boija A, Klein IA, Sabari BR, Dall'Agnese A, Coffey EL, Zamudio AV, Li CH, Shrinivas K, Manteiga JC, Hannett NM *et al* (2018) Transcription factors activate genes through the phase-separation capacity of their activation domains. *Cell* 175: 1842–1855

Bothmer A, Robbiani DF, Di Virgilio M, Bunting SF, Klein IA, Feldhahn N, Barlow J, Chen HT, Bosque D, Callen E *et al* (2011) Regulation of DNA end joining, resection, and immunoglobulin class switch recombination by 53BP1. *Mol Cell* 42: 319–329

Bracha D, Walls MT, Wei MT, Zhu L, Kurian M, Avalos JL, Toettcher JE, Brangwynne CP (2018) Mapping local and global liquid phase behavior in living cells using photo-oligomerizable seeds. *Cell* 175: 1467–1480

Brummelkamp TR, Fabius AWM, Mullenders J, Madiredjo M, Velds A, Kerkhoven RM, Bernards R, Beijersbergen RL (2006) An shRNA barcode screen provides insight into cancer cell vulnerability to MDM2 inhibitors. *Nat Chem Biol* 2: 202–206

Bunting SF, Callen E, Wong N, Chen HT, Polato F, Gunn A, Bothmer A, Feldhahn N, Fernandez-Capetillo O, Cao L *et al* (2010) 53BP1 inhibits homologous recombination in Brca1-deficient cells by blocking resection of DNA breaks. *Cell* 141: 243–254

Chapman JR, Sossick AJ, Boulton SJ, Jackson SP (2012) BRCA1-associated exclusion of 53BP1 from DNA damage sites underlies temporal control of DNA repair. *J Cell Sci* 125: 3529–3534

Cuella-Martin R, Oliveira C, Lockstone HE, Snellenberg S, Grolmusova N, Chapman JR (2016) 53BP1 integrates DNA repair and p53-dependent cell fate decisions via distinct mechanisms. *Mol Cell* 64: 51–64

Derbyshire DJ, Basu BP, Serpell LC, Joo WS, Date T, Iwabuchi K, Doherty AJ (2002) Crystal structure of human 53BP1 BRCT domains bound to p53 tumour suppressor. *EMBO J* 21: 3863–3872

Dev H, Chiang TWW, Lescale C, de Krijger I, Martin AG, Pilger D, Coates J, Sczaniecka-Clift M, Wei WM, Ostermaier M *et al* (2018) Shieldin complex promotes DNA end-joining and counters homologous recombination in BRCA1-null cells. *Nat Cell Biol* 20: 954–965

DiTullio RA, Mochan TA, Venere M, Bartkova J, Sehested M, Bartek J, Halazonetis TD (2002) 53BP1 functions in an ATM-dependent checkpoint pathway that is constitutively activated in human cancer. *Nat Cell Biol* 4: 998–1002

Dimitrova N, Chen YC, Spector DL, de Lange T (2008) 53BP1 promotes non-homologous end joining of telomeres by increasing chromatin mobility. *Nature* 456: 524–528

Drane P, Brault ME, Cui G, Meghani K, Chaubey S, Detappe A, Parnandi N, He Y, Zheng XF, Botuyan MV *et al* (2017) TIRR regulates 53BP1 by masking its histone methyl-lysine binding function. *Nature* 543: 211–216

Erdel F, Rippe K (2018) Formation of chromatin subcompartments by phase separation. *Biophys J* 114: 2262–2270

Feric M, Vaidya N, Harmon TS, Mitrea DM, Zhu L, Richardson TM, Kriwacki RW, Pappu RV, Brangwynne CP (2016) Coexisting liquid phases underlie nucleolar subcompartments. *Cell* 165: 1686–1697

Fernandez-Capetillo O, Chen HT, Celeste A, Ward I, Romanienko PJ, Morales JC, Naka K, Xia Z, Camerini-Otero RD, Motoyama N *et al* (2002) DNA damage-induced G2-M checkpoint activation by histone H2AX and 53BP1. *Nat Cell Biol* 4: 993–997

Findlay S, Heath J, Luo VM, Malina A, Morin T, Coulombe Y, Djerir B, Li Z, Samiei A, Simo-Cheyou E *et al* (2018) SHLD2/FAM35A co-operates with REV7 to coordinate DNA double-strand break repair pathway choice. *EMBO J* 37: e100158

Fong CS, Mazo G, Das T, Goodman J, Kim M, O'Rourke BP, Izquierdo D, Tsou MF (2016) 53BP1 and USP28 mediate p53-dependent cell cycle arrest in response to centrosome loss and prolonged mitosis. *Elife* 5: e16270

Ghezraoui H, Oliveira C, Becker JR, Bilham K, Moralli D, Anzilotti C, Fischer R, Deobagkar-Lele M, Sanchiz-Calvo M, Fueyo-Marcos E *et al* (2018) 53BP1 cooperation with the REV7-shieldin complex underpins DNA structure-specific NHEJ. *Nature* 560: 122–127

Giunta S, Belotserkovskaya R, Jackson SP (2010) DNA damage signaling in response to double-strand breaks during mitosis. *J Cell Biol* 190: 197–207

Gudjonsson T, Altmeyer M, Savic V, Toledo L, Dinant C, Grofte M, Bartkova J, Poulsen M, Oka Y, Bekker-Jensen S *et al* (2012) TRIP12 and UBR5 suppress spreading of chromatin ubiquitylation at damaged chromosomes. *Cell* 150: 697–709

Gupta R, Somyajit K, Narita T, Maskey E, Stanlie A, Kremer M, Typas D, Lammers M, Mailand N, Nussenzweig A *et al* (2018) DNA repair network analysis reveals shieldin as a key regulator of NHEJ and PARP inhibitor sensitivity. *Cell* 173: 972–988

Harrigan JA, Belotserkovskaya R, Coates J, Dimitrova DS, Polo SE, Bradshaw CR, Fraser P, Jackson SP (2011) Replication stress induces 53BP1-containing OPT domains in G1 cells. *J Cell Biol* 193: 97–108

Hyman AA, Weber CA, Juelicher F (2014) Liquid-liquid phase separation in biology. *Annu Rev Cell Dev Bi* 30: 39–58

Jackson SP, Bartek J (2009) The DNA-damage response in human biology and disease. *Nature* 461: 1071–1078

Joo WS, Jeffrey PD, Cantor SB, Finnin MS, Livingston DM, Pavletich NP (2002) Structure of the 53BP1 BRCT region bound to p53 and its comparison to the Brca1 BRCT structure. *Genes Dev* 16: 583–593

Jungmichel S, Stucki M (2010) MDC1: the art of keeping things in focus. *Chromosoma* 119: 337–349

Kilkenny ML, Dore AS, Roe SM, Nestoras K, Ho JC, Watts FZ, Pearl LH (2008) Structural and functional analysis of the Crb2-BRCT2 domain reveals distinct roles in checkpoint signaling and DNA damage repair. *Genes Dev* 22: 2034–2047

Kleiner RE, Verma P, Molloy KR, Chait BT, Kapoor TM (2015) Chemical proteomics reveals a gammaH2AX-53BP1 interaction in the DNA damage response. *Nat Chem Biol* 11: 807–814

Knobel PA, Belotserkovskaya R, Galanty Y, Schmidt CK, Jackson SP, Stracker TH (2014) USP28 is recruited to sites of DNA damage by the tandem BRCT domains of 53BP1 but plays a minor role in double-strand break metabolism. *Mol Cell Biol* 34: 2062–2074

Krawczyk PM, Stap J, van Oven C, Hoebe R, Aten JA (2006) Clustering of double strand break-containing chromosome domains is not inhibited by inactivation of major repair proteins. *Radiat Prot Dosimetry* 122: 150–153

Lambrus BG, Daggubati V, Uetake Y, Scott PM, Clutario KM, Sluder G, Holland AJ (2016) A USP28-53BP1-p53-p21 signaling axis arrests growth after centrosome loss or prolonged mitosis. *J Cell Biol* 214: 143–153

Larson AG, Elnatan D, Keenen MM, Trnka MJ, Johnston JB, Burlingame AL, Agard DA, Redding S, Narlikar GJ (2017) Liquid droplet formation by HP1alpha suggests a role for phase separation in heterochromatin. *Nature* 547: 236–240

Lee JH, Goodarzi AA, Jeggo PA, Paull TT (2010) 53BP1 promotes ATM activity through direct interactions with the MRN complex. *EMBO J* 29: 574–585

Lezaja A, Altmeyer M (2018) Inherited DNA lesions determine G1 duration in the next cell cycle. *Cell Cycle* 17: 24–32

Lottersberger F, Bothmer A, Robbiani DF, Nussenzweig MC, de Lange T (2013) Role of 53BP1 oligomerization in regulating double-strand break repair. *Proc Natl Acad Sci U S A* 110: 2146–2151

Lottersberger F, Karssemeijer RA, Dimitrova N, de Lange T (2015) 53BP1 and the LINC complex promote microtubule-dependent DSB mobility and DNA repair. *Cell* 163: 880–893

Lu HS, Yu D, Hansen AS, Ganguly S, Liu RD, Heckert A, Darzacq X, Zhou Q (2018) Phase-separation mechanism for C-terminal hyperphosphorylation of RNA polymerase II. *Nature* 558: 318–323

Lukas C, Savic V, Bekker-Jensen S, Doil C, Neumann B, Pedersen RS, Grofte M, Chan KL, Hickson ID, Bartek J *et al* (2011a) 53BP1 nuclear bodies form around DNA lesions generated by mitotic transmission of chromosomes under replication stress. *Nat Cell Biol* 13: 243–253

Lukas J, Lukas C, Bartek J (2011b) More than just a focus: the chromatin response to DNA damage and its role in genome integrity maintenance. *Nat Cell Biol* 13: 1161–1169

Meitinger F, Anzola JV, Kaulich M, Richardson A, Stender JD, Benner C, Glass CK, Dowdy SF, Desai A, Shiau AK *et al* (2016) 53BP1 and USP28 mediate p53 activation and G1 arrest after centrosome loss or extended mitotic duration. *J Cell Biol* 214: 155–166

Michelena J, Lezaja A, Teloni F, Schmid T, Imhof R, Altmeyer M (2018) Analysis of PARP inhibitor toxicity by multidimensional fluorescence microscopy reveals mechanisms of sensitivity and resistance. *Nat Commun* 9(1): 2678

Mirman Z, Lottersberger F, Takai H, Kibe T, Gong Y, Takai K, Bianchi A, Zimmermann M, Durocher D, de Lange T (2018) 53BP1-RIF1-shieldin counteracts DSB resection through CST- and Pol alpha-dependent fill-in. *Nature* 560: 112–116

Molliex A, Temirov J, Lee J, Coughlin M, Kanagaraj AP, Kim HJ, Mittag T, Taylor JP (2015) Phase separation by low complexity domains promotes stress granule assembly and drives pathological fibrillization. *Cell* 163: 123–133

Morales JC, Xia Z, Lu T, Aldrich MB, Wang B, Rosales C, Kellems RE, Hittelman WN, Elledge SJ, Carpenter PB (2003) Role for the BRCA1 C-terminal repeats (BRCT) protein 53BP1 in maintaining genomic stability. *J Biol Chem* 278: 14971–14977

Neumaier T, Swenson J, Pham C, Polyzos A, Lo AT, Yang P, Dyball J, Asaithamby A, Chen DJ, Bissell MJ *et al* (2012) Evidence for formation of DNA repair centers and dose-response nonlinearity in human cells. *Proc Natl Acad Sci U S A* 109: 443–448

Noon AT, Shibata A, Rief N, Lobrich M, Stewart GS, Jeggo PA, Goodarzi AA (2010) 53BP1-dependent robust localized KAP-1 phosphorylation is essential for heterochromatic DNA double-strand break repair. *Nat Cell Biol* 12: 177–184

Noordermeer SM, Adam S, Setiaputra D, Barazas M, Pettitt SJ, Ling AK, Olivieri M, Alvarez-Quilon A, Moatti N, Zimmermann M *et al* (2018) The shieldin complex mediates 53BP1-dependent DNA repair. *Nature* 560: 117–121

Ochs F, Somyajit K, Altmeyer M, Rask MB, Lukas J, Lukas C (2016) 53BP1 fosters fidelity of homology-directed DNA repair. *Nat Struct Mol Biol* 23: 714–721

Orthwein A, Fradet-Turcotte A, Noordermeer SM, Canny MD, Brun CM, Strecker J, Escribano-Diaz C, Durocher D (2014) Mitosis inhibits DNA double-strand break repair to guard against telomere fusions. *Science* 344: 189–193

Panier S, Boulton SJ (2014) Double-strand break repair: 53BP1 comes into focus. *Nat Rev Mol Cell Bio* 15: 7–18

Patel A, Lee HO, Jawerth L, Maharana S, Jahnel M, Hein MY, Stoynov S, Mahamid J, Saha S, Franzmann TM *et al* (2015) A liquid-to-solid phase transition of the ALS protein FUS accelerated by disease mutation. *Cell* 162: 1066–1077

Pellegrino S, Altmeyer M (2016) Interplay between ubiquitin, SUMO, and Poly (ADP-Ribose) in the cellular response to genotoxic stress. *Front Genet* 7: 63

Pellegrino S, Michelena J, Teloni F, Imhof R, Altmeyer M (2017) Replication-coupled dilution of H4K20me2 guides 53BP1 to pre-replicative chromatin. *Cell Rep* 19: 1819–1831

Polo SE, Jackson SP (2011) Dynamics of DNA damage response proteins at DNA breaks: a focus on protein modifications. *Gene Dev* 25: 409–433

Ran FA, Hsu PD, Wright J, Agarwala V, Scott DA, Zhang F (2013) Genome engineering using the CRISPR-Cas9 system. *Nat Protoc* 8: 2281–2308

Reyes J, Chen JY, Stewart-Ornstein J, Karhohs KW, Mock CS, Lahav G (2018) Fluctuations in p53 signaling allow escape from cell-cycle arrest. *Mol Cell* 71: 581–591 e5

Roukos V, Voss TC, Schmidt CK, Lee S, Wangsa D, Misteli T (2013) Spatial dynamics of chromosome translocations in living cells. *Science* 341: 660–664

Roy S, Musselman CA, Kachirskaia I, Hayashi R, Glass KC, Nix JC, Gozani O, Appella E, Kutateladze TG (2010) Structural insight into p53 recognition by the 53BP1 tandem tudor domain. *J Mol Biol* 398: 489–496

Sabari BR, Dall'Agnese A, Boija A, Klein IA, Coffey EL, Shrinivas K, Abraham BJ, Hannett NM, Zamudio AV, Manteiga JC *et al* (2018) Coactivator condensation at super-enhancers links phase separation and gene control. *Science* 361: eaar3958

Saredi G, Huang HD, Hammond CM, Alabert C, Bekker-Jensen S, Forne I, Reveron-Gomez N, Foster BM, Mlejnkova L, Bartke T *et al* (2016) H4K20me0 marks post-replicative chromatin and recruits the TONSL-MMS22L DNA repair complex. *Nature* 534: 714–718

Schwertman P, Bekker-Jensen S, Mailand N (2016) Regulation of DNA double-strand break repair by ubiquitin and ubiquitin-like modifiers. *Nat Rev Mol Cell Biol* 17: 379–394

Setiaputra D, Durocher D (2019) Shieldin – the protector of DNA ends. *EMBO Rep* 20: e47560

Shiloh Y, Ziv Y (2013) The ATM protein kinase: regulating the cellular response to genotoxic stress, and more. *Nat Rev Mol Cell Biol* 14: 197–210

Shin Y, Berry J, Pannucci N, Haataja MP, Toettcher JE, Brangwynne CP (2017) Spatiotemporal control of intracellular phase transitions using light-activated optodroplets. *Cell* 168: 159–171

Shin Y, Brangwynne CP (2017) Liquid phase condensation in cell physiology and disease. *Science* 357: eaaf4382

Shin Y, Chang YC, Lee DSW, Berry J, Sanders DW, Ronceray P, Wingreen NS, Haataja M, Brangwynne CP (2018) Liquid nuclear condensates mechanically sense and restructure the genome. *Cell* 175: 1481–1491 e13

Sollazzo A, Brzozowska B, Cheng L, Lundholm L, Scherthan H, Wojcik A (2018) Live dynamics of 53BP1 foci following simultaneous induction of clustered and dispersed DNA damage in U2OS cells. *Int J Mol Sci* 19: E519

Strom AR, Emelyanov AV, Mir M, Fyodorov DV, Darzacq X, Karpen GH (2017) Phase separation drives heterochromatin domain formation. *Nature* 547: 241–245

Tang J, Cho NW, Cui G, Manion EM, Shanbhag NM, Botuyan MV, Mer G, Greenberg RA (2013) Acetylation limits 53BP1 association with damaged chromatin to promote homologous recombination. *Nat Struct Mol Biol* 20: 317–325

Taslimi A, Vrana JD, Chen D, Borinskaya S, Mayer BJ, Kennedy MJ, Tucker CL (2014) An optimized optogenetic clustering tool for probing protein interaction and function. *Nat Commun* 5: 4925

Teloni F, Altmeyer M (2016) Readers of poly(ADP-ribose): designed to be fit for purpose. *Nucleic Acids Res* 44: 993–1006

Thandapani P, O'Connor TR, Bailey TL, Richard S (2013) Defining the RGG/RG motif. *Mol Cell* 50: 613–623

Toledo LI, Altmeyer M, Rask MB, Lukas C, Larsen DH, Povlsen LK, Bekker-Jensen S, Mailand N, Bartek J, Lukas J (2013) ATR prohibits replication catastrophe by preventing global exhaustion of RPA. *Cell* 155: 1088–1103

Wang B, Matsuoka S, Carpenter PB, Elledge SJ (2002) 53BP1, a mediator of the DNA damage checkpoint. *Science* 298: 1435–1438

Wang J, Choi JM, Holehouse AS, Lee HO, Zhang X, Jahnel M, Maharana S, Lemaitre R, Pozniakovsky A, Drechsel D *et al* (2018) A Molecular grammar governing the driving forces for phase separation of prion-like RNA binding proteins. *Cell* 174: 688–699 e16

Ward I, Kim JE, Minn K, Chini CC, Mer G, Chen JJ (2006) The tandem BRCT domain of 53BP1 is not required for its repair function. *J Biol Chem* 281: 38472–38477

Wegmann S, Eftekharzadeh B, Tepper K, Zoltowska KM, Bennett RE, Dujardin S, Laskowski PR, MacKenzie D, Kamath T, Commins C *et al* (2018) Tau protein liquid-liquid phase separation can initiate tau aggregation. *EMBO J* 37: e98049

Wilson MD, Durocher D (2017) Reading chromatin signatures after DNA double-strand breaks. *Philos Trans R Soc Lond B Biol Sci* 372: 20160280